Efficient Scene Recovery Using Luminous Flux Prior

Zhongyu Li [1], Lei Zhang [1] *
[1]University of Science and Technology of China, Hefei, China
ruin2@mail.ustc.edu.cn, leizh23@ustc.edu.cn,

Abstract

Scene recovery, the restoration of images degraded by adverse weather conditions, presents significant challenges for existing methods. Physical models, constrained by their inherent assumptions, often fail when these assumptions are not met; Deep learning models are powerful, they are limited by the diversity of their training datasets, leading to poor generalization and high computational demands. To address these limitations, we propose the Luminous Flux Prior (LFP), to recover degraded images under diverse adverse weather without learning. Luminous flux, a physical measure that reflects image brightness, has a rate of change that demonstrates a significant correlation with transmission. Consequently, we leverage this rate of change in luminous flux as prior knowledge to estimate transmission, which in turn assists in image recovery. This approach reduces dependency on physical parameters and enhances adaptability to various weather. Experimental validation under diverse conditions, such as sandstorms, underwater environments, and haze, attests to the robustness of LFP in restoring clear images. With a time complexity of $\mathcal{O}(N \log N)$, LFP enables real-time recovery, making it a suitable for devices with limited computational resources.

1. Introduction

Observational devices encounter significant challenges under adverse lighting conditions, which can be caused by phenomena such as sandstorms, underwater environments, and haze. These conditions lead to image degradation, typified by a loss of detail, contrast distortion, and color bias [13, 50]. Such degradation impairs computer vision tasks, including object detection [31], image segmentation [42], and scene understanding [43]. Therefore, restoring clear images from these degraded observations becomes a critical challenge in the field of computer vision [27].

Image degradation primarily arises from the scattering and absorption of light [10, 11, 16, 26, 49]. Environmental elements, such as the atmosphere and water, scatter light sources, engendering intricate environmental light and the absorption of parts of the visible light spectrum. This process significantly degrades images by diminishing their brightness. The physical quantity symbolizing the brightness per unit area, referred to as luminous flux, is denoted by F. The fundamental instigator of this degradation is a decrease in the transmission rate t, representing the proportion of light brightness received by the camera.

The challenge in image restoration is the estimation of transmission t. We bifurcate scene restoration methods into two principal types based on the calculation of t: physical models and data-driven deep learning methods. Physical models [1, 2, 16, 19, 20, 38, 54] make assumptions about the physical parameters or conditions for transmission t to be valid. However, if these assumptions fall short, the restored image suffers to varying extents. Conversely, data-driven deep learning methods extrapolate an estimation model for haze-free images from extensive datasets [3, 23, 40]. Yet, these supervised learning methods exhibit limited efficacy in real-world scenarios due to the scarcity of large-scale, diverse, and fully aligned paired training data. Additionally, deep learning algorithms necessitate complex loss functions and training strategies, resulting in high training costs [48]. Most existing methods rely solely on L1/L2 image reconstruction loss and lack robust regularization, which may induce unsuitable gradient updates and grapple with the uncertainty of ill-posed problems due to a dearth of robust prior information. Both physical models and deep learning methods find it challenging to adapt to a variety of different scenes owing to their inherent limitations [27].

Typical physical models illustrate the image formation process impacted by scattering [44]. This model can generally be represented by the following equation [36, 50]:

$$\mathbf{I}(x) = \mathbf{J}(x) \cdot t(x) + \mathbf{A}(1 - t(x)), \tag{1}$$

where x denotes the location information within the image, $\mathbf{I}(x)$ refers to the observed degraded image, $\mathbf{J}(x)$ signifies the clear image (scene radiance) we aim to restore, and $\mathbf{A}$ symbolizes the global ambient light. $t(x)$ describes the proportion of light reaching the camera. To restore a clear image $\mathbf{J}(x)$, we need to estimate the transmission $t(x)$ and

*Lei Zhang is the corresponding author.

(a) (b) (c) (d) (e) (f) (g)

Figure 1. Challenging real scene recovery using LFP. The first row depicts degraded images, while the second row presents the restored clear images. These images represent three adverse conditions: haze, sandstorm, and underwater environments. The restored images all exhibit superior visual effects. Notably, the color bias in images (b), (c), and (e) has been rectified; images (c) and (g) are free from halo artifacts; and the brightness in images (a), (b), (c), (d), and (f) has been supplemented and adjusted.

ambient light $\mathbf{A}$. $t(x)$ can be defined as:

$$t(x) = e^{-\beta d(x)}, \tag{2}$$

where β is the attenuation coefficient, indicating the degree of scattering in the environmental medium, and $d(x)$ designates the scene depth [54].

The complexity of estimating transmission lies in its dependence on multiple physical parameters [54]. Adverse weather conditions that diminish luminous flux F (detailed in Sec.3) result in image darkening, attributed to decreased t. Utilizing F directly to estimate t is impractical. We propose LFP that employs the rate of change of luminous flux, ΔF (detailed in Sec.3), as a prior to simplify the process. In extensive experimental validation, we found ΔF correlates significantly with t, thereby transforming t estimation into a ΔF computation. As a dimensionless quantity, ΔF exhibits wide applicability, underscoring the adaptability of LFP. LFP is computationally efficient and generates visually pleasing images, as demonstrated by real scenes in **Fig 1**.

In summary, our contributions are as follows:

1. We introduce a new method to estimate transmission (t), leveraging the rate of change in luminous flux (ΔF). This approach is widely applicable across different weather and imaging conditions, and does not require any learnable parameters, thus eliminating the need for dataset construction.
2. Our algorithm has a low computational complexity, $O(N \cdot \log N)$, where N is the size of a single image. With GPU acceleration, it is exceedingly fast, enhancing computation speeds by 7 to 50 times compared to CPU processing. This makes the algorithm suitable for devices with limited computational power.
3. We have transformed the estimation of t into a computation involving F and ΔF, eliminates the influence of physical parameters on t. Experimental validation confirms that this method delivers robust performance and can enhance images to a high visual quality.

2. Related Works

Physical Models: Physical models employ image statistical attributes to design priors. For instance, Dark Channel Prior (DCP) [16] utilizes the minimum value in the RGB channels of pixels. Building upon DCP, BCCR [34] introduces a more efficient method for estimating transmission coefficients. Other methods, such as Fast Visibility Restoration (FVR) [51], make assumptions about the atmospheric veil, considering it locally flat, and use median filters instead of minimum filters for transmission estimation. Color Attenuation Prior (CAP) [54] formulates a linear model between depth information and the attenuation coefficient, while ROP [27] proposes an intensity projection strategy for transmission estimation. These prior-based methods perform admirably in specific scene types, but their adaptability to diverse scenes is limited. For example, DCP tends to darken already dark areas (i.e. skies and shadows) when dehazing. To rectify this, LDCP [55] modifies sky regions. Brightness is a crucial factor for accurate transmission estimation [55], enhancing contrast and improving visual quality. Many image enhancement techniques leverage this attribute [12, 45, 52]. These algorithms typically convert RGB images to other color spaces, such as YUV and LAB, to perform color correction [45, 52], for example, HRDCP [45] and CVC [18]. In dealing with sandstorms and underwater environments, color correction methods like white balance, akin to the Gray World Hypothesis [33], are important. The hypothesis posits that the average values of the red, green, and blue channels in a scene should be approximately equal. Considering that sandstorm weather absorbs blue and green light, and underwater environments absorb red light, using color balance as prior knowledge can result in more realistic recovery effects [33].

Data-Driven Methods: Learning-based methods extrapolate models for haze-free image estimation from extensive datasets. Initial models like Waternet [25], MSCNN [40],

and AOD-Net [23], equipped with shallow architectures, outperformed previous prior-based methods. Some even incorporated prior knowledge, such as UWCNN [26] and DehazeNet [3]. Lately, most learning-based methods design more intricate and larger parameterized network architectures to enhance the network's expressivity. These include the attention mechanism [5, 7, 39], multi-scale features [6, 15, 29, 30], and even dehazing networks based on Vision Transformer (ViT) [8, 14, 53], such as gUNet [47]. Despite these advancements, the efficacy of these supervised learning methods is limited by their generalization ability in real-world scenes. The scarcity of large-scale, diverse, and fully aligned paired training data poses a significant hurdle. These methods often rely on synthetic data, but procuring synthetic data for sand and underwater environments presents challenges [28, 46]. Deep learning-based algorithms also encounter difficulties in training, requiring complex loss functions and training strategies, which lead to high training costs [48]. Many existing methods only use image reconstruction loss based on L1/L2, lacking robust regularization. This deficiency can result in unsuitable gradient updates and difficulties in grappling with the uncertainty of ill-conditioned problems, underscoring the need for robust prior information.

3. Method

In this section, we first validate the correlation between ΔF and t from a statistical perspective (Sec.3.1). Next, we derive the analytical form of transmittance using luminous flux and its rate of change (Sec.3.2). Finally, we present the numerical calculation methods for luminous flux and its rate of change, the image recovery formula and analysis of algorithmic complexity (Sec.3.3).

3.1. Luminous Flux Prior Validation

We validate the correlation between the rate of change in luminous flux, denoted as ΔF, and transmission t, utilizing datasets from three disparate weather conditions. These conditions encompass images from haze, sandstorms, and underwater environments, both simulated and real. The correlation between ΔF and t remains robust across all conditions, which underscores the utility of ΔF as a prior for image enhancement. The datasets we use are as follows:

1. **Haze:** We utilize the RESIDE dataset [24], which contains 13,990 synthetic indoor and 72,135 synthetic outdoor images.
2. **Sandstorm:** We rely on the Sand-dust Image Reconstruction Benchmark (SIRB) dataset [46], which simulates sandstorm conditions with different dust intensities.
3. **Underwater:** We employ the Underwater Image Enhancement Benchmark Dataset (UIEBD) [26] which includes 890 real underwater environment images together with reference images free of water distortion, obtained via their Deep Underwater Image Enhancement Network.

Table 1. We apply the KLD to measure the difference between the rate of change of luminance and the transmission map. Here, N symbolizes a truncated standard normal distribution, and U represents a uniform distribution within the range $[0, 1]$.

	RESIDE		SIRB			O-Haze	UIEBD
	ITS	OTS	Light	Medium	Dense		
ΔF	0.29	0.21	0.13	0.13	0.16	0.12	0.15
N	0.87	0.64	0.75	0.99	1.66	0.53	0.77
U	0.95	0.53	1.27	1.68	1.90	0.43	0.64

In total, these datasets encompass 90,960 images, comprising our entire sample space with each image representing an individual sample. For an image of size $m \times n$, denoted as $\mathbf{I}$, each pixel corresponds to three values: t, F, and ΔF. $\mathbf{T}$, $\mathbf{F}$, and $\Delta\mathbf{F}$ represent these values in matrix form. Both $\Delta\mathbf{F}$ and $\mathbf{T}$ are of the same size as image $\mathbf{I}$. $\Delta\mathbf{F} \in \mathbb{R}^{m\times n\times c}$, where c denotes the number of channels in image $\mathbf{I}$. For instance, when $\mathbf{I}$ exists in the RGB color space, $c = 3$; when $\mathbf{I}$ is a grayscale image, $c = 1$.

We employ the Kullback-Leibler Divergence (KLD) to authenticate the correlation between $\Delta\mathbf{F}$ and $\mathbf{T}$, measuring their difference as follows:

$$KLD(\Delta\mathbf{F}||\mathbf{T}) \tag{3}$$

We generate the transmission map $\mathbf{T}$ of an image by subtracting a low-quality image from a clear counterpart and taking the absolute value. The resulting image represents the degree of light scattering, with brighter regions indicating severe degradation and darker regions suggesting minor or no degradation. We temporarily disregard the effect of atmospheric light. Subsequently, we compute $\Delta\mathbf{F}$ for the degraded image and then verify the correlation between $\Delta\mathbf{F}$ and $\mathbf{T}$ using **Eq 3**.

As presented in **Tab 1**, the KLD values for $\mathbf{T}$ when using uniform or Gaussian distributions range between 0.53 to 1.66 and 0.43 to 1.90 respectively. It is important to note that the use of uniform or normal distributions does not facilitate image recovery, thus their KL values can be perceived as the upper bounds. As the KLD values inch closer to these upper bounds, image recovery becomes increasingly challenging. In contrast, the KLD values for ΔF fall within the significantly lower range of 0.12 to 0.29, approximately 4 to 10 times less than the aforementioned upper bounds. This signifying relatively low information loss when estimating $\mathbf{T}$ with $\Delta\mathbf{F}$. Therefore, $\Delta\mathbf{F}$ effectively encapsulates the characteristics of $\mathbf{T}$, indicating a pronounced correlation between $\Delta\mathbf{F}$ and $\mathbf{T}$. These findings substantiate the effectiveness of the LFP.

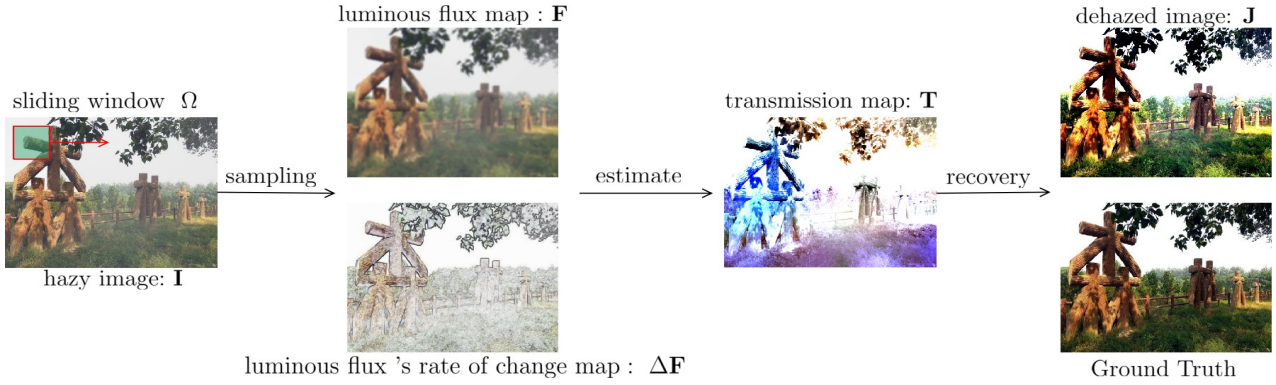

Figure 2. Visualization of the LFP Algorithm Workflow: First, it calculates Luminous Flux F and it's ratio of change ΔF within a sliding window across the image. Second, it estimates transmission t using F and ΔF. Finally, recover the image using **Eq 15**.

3.2. Scene Recovery with LFP

3.2.1 Analytical Form of Luminous Flux

The Bouguer-Lambert law [35] offers a comprehensive analytical expression for the measurement of luminous flux. This law utilizes the attenuation coefficient β[37] and the scene depth $d(x)$[21] as primary factors to accurately evaluate luminous flux **Eq 4**. In this section, to ensure clarity and simplicity, we have chosen to omit the position information denoted by x from the symbols used.

$$F = \tilde{F} e^{-\beta d} \tag{4}$$

where $\tilde{F}$ represents the luminous flux of incident light.

3.2.2 Estimating Transmission

Transmission, a property of the material, is the ratio of F to $\tilde{F}$, as depicted in **Eq 5**:

$$t = F/\tilde{F}. \tag{5}$$

In line with the Retinex [22] model, we perceive an image as composed of incident and reflected components. Incident light illuminates the object, and the object's reflected light forms the image we observe. The incident light $\tilde{F}$ can be eliminated using division, as shown in **Eq 6**:

$$t_{ij} = \frac{t_i}{t_j} = \frac{F_i/\tilde{F}_i}{F_j/\tilde{F}_j} = F_i/F_j, \tag{6}$$

where i and j represent two adjacent pixels x_i and x_j, $\tilde{F}_i = \tilde{F}j$, t_{ij} is a dimensionless parameter depicting the luminous flux F ratio between adjacent pixels. This allows analysis of flux changes within the image, crucial for revealing local features and their variations.

Based on **Eq 6**, t_{ij} can be further expressed as:

$$t_{ij} = F_i/F_j = e^{-d_i \cdot (\beta_i - \beta_j)}. \tag{7}$$

In **Eq 7**, to comprehend the influence of luminous flux on β, we introduce $\mathrm{d}\beta = \frac{\beta_i - \beta_j}{F_i - F_j}$, where $\mathrm{d}\beta$ is a differential with respect to β. By substituting $\mathrm{d}\beta$ into **Eq 7**, we obtain:

$$\begin{aligned} t_{ij} &= e^{-d_i(\beta_i - \beta_j)} \\ &= e^{-d_i(\beta_i - \beta_j)\frac{\Delta F}{\Delta F}} \\ &= e^{-d_i \cdot \Delta F \cdot \mathrm{d}\beta}. \end{aligned} \tag{8}$$

Simultaneously integrating both sides of **Eq 8**, obtain:

$$\begin{aligned} \int t \mathrm{d}t &= \int e^{-d \cdot \Delta F \cdot \mathrm{d}\beta} \\ t &= \sqrt{2e^{-d \cdot \beta \cdot \Delta F}}. \end{aligned} \tag{9}$$

The proof is provided in the appendix.

For ease of discussion, we consider $\tilde{\mathbf{F}}$ as a constant, denoted as k, where $k \in (0, 1]$. From **Eq 4**, β can be expressed as in **Eq 10**:

$$\beta = -\frac{k}{d} \log F. \tag{10}$$

By substituting **Eq 10** into **Eq 9**, we obtain the expression for t as follows:

$$\begin{aligned} t &= \sqrt{2e^{-d \cdot \beta \cdot \Delta F}} \\ &= \sqrt{2e^{\log F \cdot k \cdot \Delta F}} \\ &= \sqrt{2F^{k \Delta F}}. \end{aligned} \tag{11}$$

In **Eq 11**, we have successfully eliminated the two physical parameters $d(x)$ and β and derived an analytical form for t. Considering that the exponent part is relatively small compared to the base, **Eq 11** can be further simplified, resulting in **Eq 12**:

$$t \approx 1 + k \cdot \log F \cdot \Delta F. \tag{12}$$

In **Eq 12**, we consolidate all constants from **Eq 11** into k, where $k \in (0, 1]$, as the maximum value of luminous flux is normalized to 1. The proof is provided in the appendix.

3.3. Proposed algorithm

The numerical method for computing luminous flux, denoted as F, leverages its physical definition: the ratio of light intensity over a given area to the area itself. We implement a sliding window approach, traversing the entire image. For each window, we calculate the mean intensity and subsequently divide by the window's area to compute the numerical value of the luminous flux for each pixel. In this context, Ω represents the sliding window, $\Omega(\cdot)$ is the mean value of the samplings within the window, and S_Ω is the area of the window. Denoted as **Eq 13**:

$$F = \sum \Omega(\mathbf{I})/S_\Omega. \tag{13}$$

For numerical computation, we sample the neighborhoods of each pixel by using sliding window. Consequently, for each pixel, the ΔF can be expressed as shown in **Eq 14**:

$$\Delta F = \frac{\min \Omega(F)}{\max \Omega(F)} \tag{14}$$

We use the extreme ratio within the sliding window to amplify ΔF because the difference between adjacent pixels is close to 0. However, ΔF might be affected by noise. To mitigate this, we first truncate $\Omega(F)$ within the range $[0.005, 0.95]$. Following this, it may be necessary to truncate the transmission t during subsequent processing to ensure stability and accuracy in our results.

In recovery process, we define a clear image $\mathbf{J}$ using an image formulation model from **Eq 1**. This is expressed as follows in **Eq 15**:

$$\mathbf{J}(x) = \frac{\mathbf{I}(x) + \mathbf{A}\omega(t(x) - 1)}{\max(\omega t(x), t_0)}. \tag{15}$$

In **Eq 15**, ω is a constant relaxation parameter which is constrained to be in the range $(0, 1]$, and t_0, set as 0.05, is a lower bound that provides stability during computation.

The global atmospheric light, represented by $\mathbf{A}$, plays a crucial role in our model. We estimate $\mathbf{A}$ swiftly using a two-step approach. Initially, $\mathbf{A}$ is estimated using mean filtering and the maximum grayscale value of the original image. This gives us an initial approximation of the global atmospheric light. Subsequently, the image is segmented into small regions, and we select the maximum value from each region to represent the $\mathbf{A}$ for that particular region. The final estimate of $\mathbf{A}$ is then calculated as the average of all the $\mathbf{A}$ values from these small regions. This method allows us to get a more refined and accurate estimate of the global atmospheric light. The complete process of our scene recovery method is thoroughly depicted in **Fig 2**, and the corresponding pseudo-code is provided in Algorithm 1. In terms of computational complexity, our algorithm starts off with a complexity of $\mathcal{O}(N)$ as we traverse all pixels in the image using a sliding window. Then, it rises by $\mathcal{O}(\log N)$ when we compute the maximum and minimum values for each window. Finally, the total computational complexity for the subsequent steps, which include the calculation of transmission according to **Eq 11** and application of a guided filter [17] for smoothing, is $\mathcal{O}(N \log N)$, where N denotes the size of a single image. This complexity analysis demonstrates that our method is efficient and feasible for large scale image recovery tasks.

Algorithm 1 Pseudo-code for LFP

Setup: constant $k = 0.5$ and window size $\Omega = 7$
Input: Degraded image I
while Ω in I **do** ▷ sliding window traversal
    Compute mean intensity: $I_\Omega = \sum \Omega(I)/S_\Omega$
    Compute luminous flux: $F = I_\Omega/S_\Omega$
    Compute rate of change: $\Delta F = \frac{\min \Omega(F)}{\max \Omega(F)}$
end while
$t \approx 1 + k \cdot \log F \cdot \Delta F$ ▷ Compute the transmission
guided filtering on transmission
Output: $J = \frac{I + A \cdot (t-1)}{t}$ ▷ recover the scene

Figure 3. Visual comparisons of different dehazing methods on outdoor and indoor images. The algorithms designed for water removal (blue) and sand removal (yellow-brown) fail in haze (grey) environments. Our method effectively restores details in the sky region without introducing artifacts. It also improves the visual quality of indoor images by enhancing brightness while preserving the structure.

4. Experiments

4.1. Implementation Details

Our method relies solely on two parameters: k and the sliding window Ω. And uses a non-parametric approach for the estimation of transmission t, enhancing visual results under a variety of visibility conditions. Based on empirical experiences, we have determined the optimal settings to be $k = 0.5$ and $\Omega = 7$. All experiments were conducted on a machine with an AMD Ryzen 7 3750H CPU@2.3GHz and a GeForce RTX 2080 GPU (11GB). The deep learning models were built with the PyTorch, TensorFlow and Matlab frameworks. The test images are publicly available.

4.2. Experimental Settings

We evaluated the LFP's performance using various methods and datasets, including physical models and deep learning models. Selected datasets spanned varied environments and scattering degrees, including RESIDE [24], SIRB [46], UIEBD [26], Haze4K [32], and RS-Haze [24]. These encompassed synthetic to real-world scenes, ensuring broad evaluation robustness. We used Peak Signal-to-Noise Ratio (PSNR) and Structural Similarity Index Measure (SSIM) metrics for objective and fair evaluations across scenarios and methods.

4.3. Qualitative Comparison

Image Dehazing. We use RESIDE dataset [24] to validate the efficacy and robustness of LFP, as is shown in **Fig 3**, by comparing it with Dive+ and HRDCP. While Dive+ fails to restore image clarity, HRDCP results in color deviation, likely due to the specific absorption and scattering properties of sand particles. In contrast, our LFP method can generate more natural-looking results with better structures in a more stable manner. This demonstrates that images in hazy and underwater environments are formed based on different optical properties. We then compare the performance of the LFP with different methods like MSCNN, gUNet, and DCP. Learning-based methods such as gUNet and MSCNN are susceptible to dataset bias, which makes it difficult to enhance visual quality. Meanwhile, traditional methods like DCP, which rely on hand-crafted priors, struggle with varied real-world conditions. LFP adeptly overcomes the major obstacle faced by previous dehazing approaches, which is the problematic influence of scene depth. The inherent uncertainty in depth estimation often leads to unstable performance. By confidently deriving the relationship between ΔF and t without involving d, LFP successfully avoids the dataset bias that learning-based methods encounter. LFP effectively bypasses complex parameters of transmission and offers reliable solution with robust theoretical guarantees. Our method demonstrates a significantly stronger capability for robust image restoration in hazy weather conditions, resulting in highly satisfactory visual results.

Underwater Image Enhancement. We validate the efficacy and robustness of LFP for underwater image enhancement through comprehensive experiments, using UIEBD dataset [26]. Results are shown in **Fig 4**. We first compare it with DCP and HRDCP, which are methodologies designed for different weather conditions. DCP fails completely, and although HRDCP achieves some visual effects, it suffers from noticeable color distortion. These experimental results underscore the necessity for image processing techniques to be specifically designed and optimized for each environment, reinforcing that an algorithm effective in one environment can't simply be applied to another without adaptation. Dive+ and UWCNN struggle to effectively eliminate the green light prevalent in underwater scenes, leading to undesired color shifts. Although Waternet and ROP perform well in color restoration, they both suffer from dimmed lighting and reduced contrast, thereby compromising the overall visual quality. LFP overcomes the major obstacle faced by previous underwater image enhancement approaches, which is the varying influence of the attenuation coefficient β on the RGB color channels that often results in color bias. By eliminating the attenuation coefficient β during the derivation process, LFP avoids the color bias, rendering it a reliable solution with robust theoretical guarantees. Therefore, LFP method demonstrates competitive color correction and contrast enhancement capabilities.

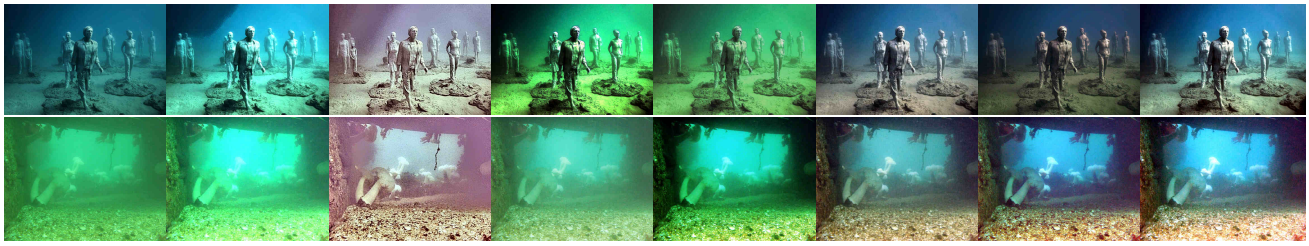

Figure 4. Comparison of different methods for underwater conditions. The algorithms designed for haze removal (grey) and sand removal (brown) fail in underwater (blue) environments. Our method corrects color shifts, enhance image brightness and improve visibility.

Figure 5. Comparison of different methods for sandstorm image enhancement. The algorithms designed for haze removal (grey) and water removal (blue) fail in sandstorm (brown) environments. Our method corrects color shifts, enhances image brightness, and improves contrast, resulting in more vibrant color reproduction. Moreover, LFP produces a more realistic sky area closer to real scenes.

Visibility Restoration in Sandstorms. We assess our LFP method's effectiveness in restoring visibility during sandstorms, by using SIRB dataset [46]. Results are shown in **Fig 5**. Initially, we compare LFP's performance with DCP, MSCNN, and Dive+. The first two fail in dust and sandstorm mitigation, and Dive+ introduces noticeable color deviations in sky areas. This emphasizes that hazy and sandstorm images are influenced by distinct optical properties, making dehaze or dewater algorithms unsuitable for sandstorms. Next, we contrast our method with CVC, HRDCP, and ROP. All three significantly enhance visibility in sandstorms. However, CVC lacks contrast, leading to detail loss. HRDCP, despite its visual improvements, exhibits a dim sky and color distortions due to its DCP-based design. ROP performs well but struggles with color distortion, resulting in a cool appearance. LFP overcomes prior challenges by addressing scene depth and attenuation coefficient β. By eliminating hard-to-estimate parameters like atmospheric light and scene depth, LFP avoids common issues, making it robust in sandstorm conditions without relying on assumptions. Thus, our LFP method excels in sandstorm image restoration, producing visually pleasing results without color distortion.

In summary, the LFP has the ability to restore scenes in a variety of severe weather conditions, a characteristic that is absent in most algorithms. By eliminating the physical parameters that impact transmittance, LFP effectively bypasses the influence of scene depth, thus enhancing visual quality. Moreover, it minimizes color deviations by removing the attenuation coefficient. This approach provides a theoretically and empirically supported a priori method for scene restoration algorithms.

4.4. Quantitative Comparison

Dehazing Quality We selected DCP, BCCR [34], and FVR [51] as our benchmarks to represent different types of prior-based dehazing methodologies. The rationale behind this selection, instead of opting for deep learning techniques, is multi-fold. Traditional dehazing methods not only possess the capability to restore clear images, but they also notably improve visual effects, thereby enhancing the visual experience. Furthermore, LFP does not contain any learnable parameters, differentiating it from deep learning approaches. As illustrated in **Tab 2**, demonstrates that LFP outperforms other methods across all four of our test datasets.

Table 2. This table succinctly presents the comparative results of the LFP method and three other distinct prior methods. The evaluation spans across all datasets and metrics, with LFP consistently achieving superior performance. The highest PSNR and SSIM values, represented by **bold** text, clearly demonstrate the effectiveness of our LFP method.

Methods	RESIDE-IN		RESIDE-OUT		Haze-4K		RS-Haze	
	PSNR	SSIM	PSNR	SSIM	PSNR	SSIM	PSNR	SSIM
DCP	16.62	0.818	19.13	0.815	14.01	0.760	17.86	0.734
BCCR	16.88	0.791	14.02	0.777	13.78	0.756	18.84	0.747
FVR	15.72	0.748	11.61	0.668	12.65	0.688	16.12	0.626
LFP	**19.76**	**0.869**	**21.05**	**0.861**	**18.29**	**0.873**	**18.24**	**0.786**

The performance is consistent whether we evaluate in terms of PSNR or SSIM. This robust evidence strongly validates the high generalization ability of the LFP method. Furthermore, the LFP method excels in restoring clear, detailed imagery, as particularly demonstrated by the significant improvement in SSIM scores. For more detailed results on desanding and dewatering, please refer to the appendix.

Runtime Efficiency We conducted extensive comparisons on both CPU and GPU platforms. On the CPU, we compared LFP with traditional dehazing methods; on the GPU, we chose a variety of deep learning dehazing models, including: MSCNN, AOD-Net [23], GFN [41], GCANet [4], GDNet [30], MSBDN [6], FFA [39], CycleD [9], DehazeF [47], and gUNet-T. In terms of runtime, **Tab 3** compares the efficiency on both CPU and GPU. The results show that the LFP method consistently achieves the fastest running speed, surpassing existing algorithms.

CPU Performance. As evidenced by the data presented in **Tab 3**, the LFP model consistently exhibits superior runtime performance across all tested resolutions. With a runtime of merely 0.007 seconds at the lower-end resolution of 360p, and a still impressive 0.863 seconds at the high-end 4k resolution, these empirical findings underscore the remarkable efficiency of the LFP model when processing large-scale images or performing real-time scene recovery.

Table 3. **Run-time(seconds) performance**. Testing the efficiency of different methods on various single image sizes. Models marked with (*) indicate that the results for those models were generated using MATLAB.The best performance is denoted in red, while the second best performance is indicated in blue.

CPU Performance						
Model	**360p**	**480p**	**720p**	**1080p**	**2k**	**4k**
DCP[16]	0.459	0.765	1.76	2.600	6.74	15.11
Retinex[22]	0.149	0.286	0.478	0.804	2.367	5.421
LDCP[55]	0.517	0.821	2.205	3.091	8.264	18.09
CAP[54]	0.218	0.310	0.666	1.021	2.866	6.403
BCCR[34]	1.691	3.571	6.416	11.70	29.60	64.26
FVR[51]	0.301	3.902	8.589	12.58	34.35	76.50
ROP*[27]	0.067	0.144	0.411	1.399	2.073	2.515
LFP	0.007	0.017	0.073	0.151	0.407	0.863
GPU Performance						
MSCNN[40]	0.115	0.147	0.266	0.462	1.114	2.481
DehazeNet[3]	0.165	0.223	0.405	0.621	1.374	2.951
AOD-Net[23]	0.076	0.106	0.175	0.291	0.696	1.519
GFN*[41]	0.660	0.858	1.494	2.445	6.353	13.09
GCANet[4]	0.446	0.641	1.107	1.821	4.262	9.266
GDNet[30]	0.644	0.742	1.503	2.027	4.675	10.48
MSBDN[6]	0.952	1.212	2.194	3.335	8.203	17.46
FFA[39]	1.675	2.253	3.960	5.977	14.27	30.61
CycleD[9]	0.607	0.810	1.428	2.158	5.155	11.03
DehazeF[47]	0.289	0.387	0.677	1.032	2.475	5.310
gUNet-T[47]	0.197	0.266	0.473	0.716	1.719	3.669
ROP*[27]	0.047	0.051	0.113	0.209	0.532	0.894
LFP	0.001	0.001	0.002	0.003	0.008	0.019

GPU Performance. **Tab 3** shows that LFPsignificantly outperforms all the compared algorithms in processing speed, especially for high-resolution images. For instance, at a resolution of 4K, LFP's average runtime is merely 0.019 seconds, whereas the runtimes of other algorithms range from 0.894 seconds to a staggering 30.609 seconds. This results in a speedup of up to 34 times for LFP, marking its superior computational efficiency.

4.5. Ablation Study on k and Ω

Our ablation study further reveals that the changes in the k parameter not only influence the luminous flux rate of change ΔF but also directly affect the transmission estimation. A properly tuned k facilitates an accurate estimation of the transmission map, thus effectively reducing the impact of different weather conditions on the image. On the other hand, the size of the sliding window Ω directly affects the local variance ΔF. A larger Ω captures more significant changes in the luminous flux, which is particularly effective in dense haze conditions or when the scene has a greater depth of view. This broadened perspective allows for a more comprehensive understanding of the scene, leading to a higher-quality image after enhancement. Finally, the interplay between k and Ω is also crucial. Balancing these two factors allows for a fine-tuned approach to image enhancement, taking into account both the overall brightness and the local variance of the image, this ability to cope with complex conditions adds another layer of robustness to our technique. This balance ensures that the final output image is visually pleasing while maintaining the fidelity of the original scene.

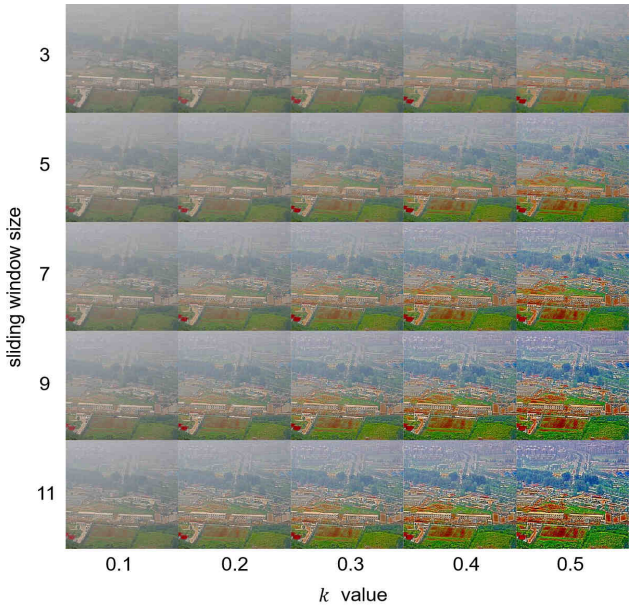

Figure 6. The x-axis represents k, the y-axis represents Ω. When the depth of view is further, or the haze is denser, Ω and k need to be increased correspondingly.

5. Conclusion

In this work, we propose an efficient scene recovery algorithm to restore clear images under poor visibility conditions. By analyzing the image formation model, we derive an analytical form for transmission that eliminates multiple influencing factors and leverages the correlation with flux change rate as prior knowledge. Our approach achieves state-of-the-art performance while maintaining low computational complexity, enabling real-time processing on resource-limited devices. Extensive experiments validate the effectiveness of the proposed method. The novel integration of prior knowledge and analytical transmission modeling provides opportunities to inform future learning-based methods. Overall, this paper makes significant contributions towards robust scene recovery under challenging imaging conditions.

6. Acknowledgments

This work was supported by the National Natural Science Foundation of China (No. 62336001,No. 62072014)

References

[1] Dana Berman, Shai Avidan, et al. Non-local image dehazing. In *Proceedings of the IEEE conference on computer vision and pattern recognition*, pages 1674–1682, 2016. 1

[2] Trung Minh Bui and Wonha Kim. Single image dehazing using color ellipsoid prior. *IEEE Transactions on Image Processing*, 27(2):999–1009, 2017. 1

[3] Bolun Cai, Xiangmin Xu, Kui Jia, Chunmei Qing, and Dacheng Tao. Dehazenet: An end-to-end system for single image haze removal. *IEEE Transactions on Image Processing*, 25(11):5187–5198, 2016. 1, 3, 8

[4] Dongdong Chen, Mingming He, Qingnan Fan, Jing Liao, Liheng Zhang, Dongdong Hou, Lu Yuan, and Gang Hua. Gated context aggregation network for image dehazing and deraining. In *2019 IEEE winter conference on applications of computer vision (WACV)*, pages 1375–1383. IEEE, 2019. 7, 8

[5] Qili Deng, Ziling Huang, Chung-Chi Tsai, and Chia-Wen Lin. Hardgan: A haze-aware representation distillation gan for single image dehazing. In *European Conference on Computer Vision*, pages 722–738. Springer, 2020. 3

[6] Hang Dong, Jinshan Pan, Lei Xiang, Zhe Hu, Xinyi Zhang, Fei Wang, and Ming-Hsuan Yang. Multi-scale boosted dehazing network with dense feature fusion. In *Proceedings of the IEEE/CVF Conference on Computer Vision and Pattern Recognition*, pages 2157–2167, 2020. 3, 7, 8

[7] Jiangxin Dong and Jinshan Pan. Physics-based feature dehazing networks. In *European Conference on Computer Vision*, pages 188–204. Springer, 2020. 3

[8] Alexey Dosovitskiy, Lucas Beyer, Alexander Kolesnikov, Dirk Weissenborn, Xiaohua Zhai, Thomas Unterthiner, Mostafa Dehghani, Matthias Minderer, Georg Heigold, Sylvain Gelly, et al. An image is worth 16x16 words: Transformers for image recognition at scale. *arXiv preprint arXiv:2010.11929*, 2020. 3

[9] Deniz Engin, Anil Genç, and Hazim Kemal Ekenel. Cycle-dehaze: Enhanced cyclegan for single image dehazing. In *Proceedings of the IEEE Conference on Computer Vision and Pattern Recognition Workshops*, pages 825–833, 2018. 7, 8

[10] Faming Fang, Fang Li, and Tieyong Zeng. Single image dehazing and denoising: a fast variational approach. *SIAM Journal on Imaging Sciences*, 7(2):969–996, 2014. 1

[11] Xueyang Fu, Yue Huang, Delu Zeng, Xiao-Ping Zhang, and Xinghao Ding. A fusion-based enhancing approach for single sandstorm image. In *2014 IEEE 16th international workshop on multimedia signal processing (MMSP)*, pages 1–5. IEEE, 2014. 1

[12] Han Gao, Ping Wei, and Jun Ke. Color enhancement and image defogging in hsi based on retinex model. In *2015 International Conference on Optical Instruments and Technology: Optoelectronic Imaging and Processing Technology*, pages 9–16. SPIE, 2015. 2

[13] Jie Gui, Xiaofeng Cong, Yuan Cao, Wenqi Ren, Jun Zhang, Jing Zhang, Jiuxin Cao, and Dacheng Tao. A comprehensive survey and taxonomy on single image dehazing based on deep learning. *ACM Computing Surveys*, 55(13s):1–37, 2023. 1

[14] Chun-Le Guo, Qixin Yan, Saeed Anwar, Runmin Cong, Wenqi Ren, and Chongyi Li. Image dehazing transformer with transmission-aware 3d position embedding. In *Proceedings of the IEEE/CVF Conference on Computer Vision and Pattern Recognition*, pages 5812–5820, 2022. 3

[15] Yecai Guo, Hanyu Li, and Peixian Zhuang. Underwater image enhancement using a multiscale dense generative adversarial network. *IEEE Journal of Oceanic Engineering*, 45(3):862–870, 2019. 3

[16] Kaiming He, Jian Sun, and Xiaoou Tang. Single image haze removal using dark channel prior. *IEEE transactions on pattern analysis and machine intelligence*, 33(12):2341–2353, 2010. 1, 2, 8

[17] Kaiming He, Jian Sun, and Xiaoou Tang. Guided image filtering. *IEEE transactions on pattern analysis and machine intelligence*, 35(6):1397–1409, 2012. 5

[18] Jong-Ju Jeon, Tae-Hee Park, and Il-Kyu Eom. Sand-dust image enhancement using chromatic variance consistency and gamma correction-based dehazing. *Sensors*, 22(23):9048, 2022. 2

[19] Mingye Ju, Can Ding, Y Jay Guo, and Dengyin Zhang. Idgcp: Image dehazing based on gamma correction prior. *IEEE Transactions on Image Processing*, 29:3104–3118, 2019. 1

[20] Manjit Kaur, Dilbag Singh, Vijay Kumar, and Kehui Sun. Color image dehazing using gradient channel prior and guided l0 filter. *Information Sciences*, 521:326–342, 2020. 1

[21] Johannes Kopf, Boris Neubert, Billy Chen, Michael Cohen, Daniel Cohen-Or, Oliver Deussen, Matt Uyttendaele, and Dani Lischinski. Deep photo: Model-based photograph enhancement and viewing. *ACM transactions on graphics (TOG)*, 27(5):1–10, 2008. 4

[22] Edwin H Land. The retinex theory of color vision. *Scientific american*, 237(6):108–129, 1977. 4, 8

[23] Boyi Li, Xiulian Peng, Zhangyang Wang, Jizheng Xu, and Dan Feng. Aod-net: All-in-one dehazing network. In *Proceedings of the IEEE international conference on computer vision*, pages 4770–4778, 2017. 1, 3, 7, 8

[24] Boyi Li, Wenqi Ren, Dengpan Fu, Dacheng Tao, Dan Feng, Wenjun Zeng, and Zhangyang Wang. Benchmarking single-image dehazing and beyond. *IEEE Transactions on Image Processing*, 28(1):492–505, 2019. 3, 6

[25] Chongyi Li, Chunle Guo, Wenqi Ren, Runmin Cong, Junhui Hou, Sam Kwong, and Dacheng Tao. An underwater image enhancement benchmark dataset and beyond. *IEEE Transactions on Image Processing*, 29:4376–4389, 2019. 2

[26] Chongyi Li, Saeed Anwar, and Fatih Porikli. Underwater scene prior inspired deep underwater image and video enhancement. *Pattern Recognition*, 98:107038, 2020. 1, 3, 6

[27] Jun Liu, Wen Liu, Jianing Sun, and Tieyong Zeng. Rank-one prior: Toward real-time scene recovery. In *Proceedings of the IEEE/CVF Conference on Computer Vision and Pattern Recognition*, pages 14802–14810, 2021. 1, 2, 8

[28] Risheng Liu, Xin Fan, Ming Zhu, Minjun Hou, and Zhongxuan Luo. Real-world underwater enhancement: Challenges, benchmarks, and solutions under natural light. *IEEE transactions on circuits and systems for video technology*, 30(12): 4861–4875, 2020. 3

[29] Xiaodong Liu, Zhi Gao, and Ben M Chen. Mlfcgan: Multilevel feature fusion-based conditional gan for underwater image color correction. *IEEE Geoscience and Remote Sensing Letters*, 17(9):1488–1492, 2019. 3

[30] Xiaohong Liu, Yongrui Ma, Zhihao Shi, and Jun Chen. Griddehazenet: Attention-based multi-scale network for image dehazing. In *Proceedings of the IEEE/CVF International Conference on Computer Vision*, pages 7314–7323, 2019. 3, 7, 8

[31] Yu Liu, Guanlong Zhao, Boyuan Gong, Yang Li, Ritu Raj, Niraj Goel, Satya Kesav, Sandeep Gottimukkala, Zhangyang Wang, Wenqi Ren, et al. Improved techniques for learning to dehaze and beyond: A collective study. *arXiv preprint arXiv:1807.00202*, 2018. 1

[32] Ye Liu, Lei Zhu, Shunda Pei, Huazhu Fu, Jing Qin, Qing Zhang, Liang Wan, and Wei Feng. From synthetic to real: Image dehazing collaborating with unlabeled real data. In *Proceedings of the 29th ACM International Conference on Multimedia*, pages 50–58, 2021. 6

[33] Rastislav Lukac. *Single-sensor imaging: methods and applications for digital cameras*. CRC Press, 2018. 2

[34] Gaofeng Meng, Ying Wang, Jiangyong Duan, Shiming Xiang, and Chunhong Pan. Efficient image dehazing with boundary constraint and contextual regularization. In *Proceedings of the IEEE international conference on computer vision*, pages 617–624, 2013. 2, 7, 8

[35] WE Knowles Middleton. Bouguer, lambert, and the theory of horizontal visibility. *Isis*, 51(2):145–149, 1960. 4

[36] Srinivasa G Narasimhan and Shree K Nayar. Vision and the atmosphere. *International journal of computer vision*, 48(3): 233–254, 2002. 1

[37] Srinivasa G Narasimhan and Shree K Nayar. Interactive (de) weathering of an image using physical models. In *IEEE Workshop on color and photometric Methods in computer Vision*, page 1. France, 2003. 4

[38] Ko Nishino, Louis Kratz, and Stephen Lombardi. Bayesian defogging. *International journal of computer vision*, 98(3): 263–278, 2012. 1

[39] Xu Qin, Zhilin Wang, Yuanchao Bai, Xiaodong Xie, and Huizhu Jia. Ffa-net: Feature fusion attention network for single image dehazing. In *Proceedings of the AAAI Conference on Artificial Intelligence*, pages 11908–11915, 2020. 3, 7, 8

[40] Wenqi Ren, Si Liu, Hua Zhang, Jinshan Pan, Xiaochun Cao, and Ming-Hsuan Yang. Single image dehazing via multi-scale convolutional neural networks. In *European conference on computer vision*, pages 154–169. Springer, 2016. 1, 2, 8

[41] Wenqi Ren, Lin Ma, Jiawei Zhang, Jinshan Pan, Xiaochun Cao, Wei Liu, and Ming-Hsuan Yang. Gated fusion network for single image dehazing. In *Proceedings of the IEEE Conference on Computer Vision and Pattern Recognition*, pages 3253–3261, 2018. 7, 8

[42] Wenqi Ren, Jingang Zhang, Xiangyu Xu, Lin Ma, Xiaochun Cao, Gaofeng Meng, and Wei Liu. Deep video dehazing with semantic segmentation. *IEEE Transactions on Image Processing*, 28(4):1895–1908, 2018. 1

[43] Christos Sakaridis, Dengxin Dai, Simon Hecker, and Luc Van Gool. Model adaptation with synthetic and real data for semantic dense foggy scene understanding. In *Proceedings of the European Conference on Computer Vision (ECCV)*, pages 687–704, 2018. 1

[44] Yoav Y Schechner and Yuval Averbuch. Regularized image recovery in scattering media. *IEEE Transactions on Pattern Analysis and Machine Intelligence*, 29(9):1655–1660, 2007. 1

[45] Zhenghao Shi, Yaning Feng, Minghua Zhao, Erhu Zhang, and Lifeng He. Let you see in sand dust weather: A method based on halo-reduced dark channel prior dehazing for sand-dust image enhancement. *Ieee Access*, 7:116722–116733, 2019. 2

[46] Yazhong Si, Fan Yang, Ya Guo, Wei Zhang, and Yipu Yang. A comprehensive benchmark analysis for sand dust image reconstruction. *Journal of Visual Communication and Image Representation*, 89:103638, 2022. 3, 6, 7

[47] Yuda Song, Zhuqing He, Hui Qian, and Xin Du. Vision transformers for single image dehazing. *arXiv preprint arXiv:2204.03883*, 2022. 3, 7, 8

[48] Yuda Song, Yang Zhou, Hui Qian, and Xin Du. Rethinking performance gains in image dehazing networks. *arXiv preprint arXiv:2209.11448*, 2022. 1, 3

[49] Matan Sulami, Itamar Glatzer, Raanan Fattal, and Mike Werman. Automatic recovery of the atmospheric light in hazy images. In *2014 IEEE International Conference on Computational Photography (ICCP)*, pages 1–11. IEEE, 2014. 1

[50] Robby T Tan. Visibility in bad weather from a single image. In *2008 IEEE Conference on Computer Vision and Pattern Recognition*, pages 1–8. IEEE, 2008. 1

[51] Jean-Philippe Tarel and Nicolas Hautiere. Fast visibility restoration from a single color or gray level image. In *2009 IEEE 12th International Conference on Computer Vision*, pages 2201–2208. IEEE, 2009. 2, 7, 8

[52] Ting Yan, Liejun Wang, and Jiaxing Wang. Method to enhance degraded image in dust environment. *J. Softw.*, 9(10): 2672–2677, 2014. 2

[53] Dong Zhao, Jia Li, Hongyu Li, and Long Xu. Hybrid local-global transformer for image dehazing. *arXiv preprint arXiv:2109.07100*, 2021. 3

[54] Qingsong Zhu, Jiaming Mai, and Ling Shao. A fast single image haze removal algorithm using color attenuation prior. *IEEE transactions on image processing*, 24(11):3522–3533, 2015. 1, 2, 8

[55] Yingying Zhu, Gaoyang Tang, Xiaoyan Zhang, Jianmin Jiang, and Qi Tian. Haze removal method for natural restoration of images with sky. *neurocomputing*, 275:499–510, 2018. 2, 8